Quantitative assessment of the structure and bonding properties of 50VxOy-50P2O5 glass by classical and Born–Oppenheimer molecular dynamics

Steve Dave Wansi Wendji, Carlo Massobrio, Mauro Boero, Christine Tugene, Elena Levchenko, Firas Shuaib, Rémi Piotrowski, David Hamani, Gaelle Delaizir, Pierre-Marie Geffroy, et al.

Quantitative assessment of the structure and bonding properties of $50V_xO_y$-$50P_2O_5$ glass by classical and Born-Oppenheimer molecular dynamics

S.D. Wansi Wendji[a], C. Massobrio[a], M. Boero[a], C. Tugène[a], E. Levchenko[b], F. Shuaib[c], R. Piotrowski[c], D. Hamani[c], G. Delaizir[c], P.-M. Geffroy[c], P. Thomas[c], O. Masson[c], A. Bouzid[c], G. Ori*[a]

[a]*Université de Strasbourg, CNRS, Institut de Physique et Chimie des Matériaux de Strasbourg, UMR 7504, F-67034 Strasbourg, France*
[b]*School of Information and Physical Sciences, The University of Newcastle, Callaghan, NSW 2308, Australia*
[c]*Institut de Recherche sur les Céramiques, UMR 7315 CNRS-Univesité de Limoges, Centre Européen de la Céramique, 12 rue Atlantis 87068 Limoges Cedex, France*

Abstract

The structure and bonding of V_xO_y–P_2O_5 (VP50) glass is studied by atomistic modeling. We performed an in-depth analysis of the structure and chemical bonding properties of VP50 glass by classical and Born-Oppenheimer molecular dynamics (CMD and BOMD). Through a thorough comparison with experimental data, our study showcases the effectiveness of BOMD in addressing the shortcomings of CMD and achieves a significantly improved and superior quantitative description of VP50 glass' structures. BOMD allows us to achieve an unprecedented agreement with experimental data in terms of both reciprocal space (neutron and X-ray structure factors) and real space (total pair correlation functions) properties. The key improvement is ascribed to a better description of the local electronic and bonding environment around both P and, especially, V sites that can not be obtained by empirical force fields. A clear signature of single V–O and double V=O bonds is found with BOMD together with an overall better description of VO_n coordinating polyhedra distribution that constitute the network of this glass. Our study is enriched by a thorough analysis of bond angle distributions around VO_n units, order and connectivity parameters and local bonding features based on Wannier functions formalism. All together, the results found define the computational grounds for a deep understating of VP amorphous glasses in conjunctions with depicting the necessary requirements for the development of interatomic potentials aiming to a quantitative comprehension and design of VP-based amorphous materials.

Keywords: Atomistic modeling, BOMD, Vanadophosphates glasses

1. Introduction

Silicate and phosphate glasses containing vanadium or iron oxides are promising materials for solid-state batteries and electrochemical storage devices due to their physical and chemical properties, such as high glass-forming ability, wide vitrification range, low glass transition temperature, low melting point and high thermal expansion coefficients [1, 2]. These glasses have also demonstrated enhanced energy density performance, due to their ability to promote multi-electron reactions [1–3]. Vanado-phosphate (VP) glasses, in particular, have been studied as cathode materials for ion batteries, owing to their multiple oxidation states and capability to stand multiple cycles [4–8].
The wide range of applications of VP glasses has motivated numerous experimental studies, employing techniques such as X-rays and Neutrons diffraction [9–11], Raman Spectroscopy [12], Nuclear Magnetic Resonance (NMR) [13, 14], X-ray Photoelectron Spectroscopy (XPS) [15], Infrared Spectroscopy (IR) [16], Extended X-ray Absorption Fine Structure (EXAFS) [17, 18], and X-ray Absorption Near-Edge Structure (XANES) [15, 18, 19]. The coexistence of different oxidation states such as V^{5+}, V^{4+} and V^{3+} with four, five or six-fold coordination gives rise to a structure characterized by the presence of a large variety of structural units in the glass network [9, 16]. For these reasons, precise atomic-scale characterization has been challenging, motivating the use of quantitative modelling tools to better understand the topology of these amorphous systems.

Classical molecular dynamics (CMD) [8, 15, 20–24], non-constant force field MD (ncMD) [16] and reverse

Email address: guido.ori@ipcms.unistra.fr (G. Ori*)

Monte Carlo (RMC) simulations [9–11, 25] have been predominantly employed on VP glasses and alkali-ion-containing VP glasses. Nevertheless, an exhaustive comparison with experimental data is lacking since a determination of the local coordination environment of V sites remains a major challenge. One of the key issues is related to the identity of the coordination state of V ions, in relationship with V sites other than V^{5+} (V^{4+} and V^{3+}) conferring a (para)magnetic character to the system and preventing the use of some experimental techniques [14]. An additional source of debate stems from the existence of V^{4+} in four-fold coordination in silicate and phosphate glasses [15, 26, 27]. For instance, XPS and XANES measurements provided evidence for the presence of V^{4+} in four-fold coordination in aluminoborosilicate glasses containing high vanadium content [15]. Similarly, in VP glasses, 1D/2D $^{31}P/^{31}V$ magic angle spinning NMR techniques and advanced pulsed electron paramagnetic resonance (EPR) [13] pointed toward V^{4+} ions in four-fold coordination. Along these lines, CMD results were found consistent with the presence of V^{4+} ions in tetrahedral coordination in both silicate and phosphate glasses [15, 21, 28]. However, in amorphous Na_2O-V_xO_y-P_2O_5 [29] and crystalline vanadium oxides and VP systems [19, 30–32], V^{4+} four-fold coordination is not found, and only V^{5+} is widely reported to be able to accommodate the tetrahedral coordination. Therefore, it appears that the lack of agreement between experiments and theory calls for further predictive calculations improving our knowledge of the coordination state of V in vanadophosphate glasses.

With this purpose in mind, we use in this study classical molecular dynamics (CMD) and first-principles molecular dynamics (in the Born-Oppenheimer version, BOMD) simulations to investigate the structure of $50V_xO_y$-$50P_2O_5$ vanadophosphate glass (referred to hereafter as VP50). Based on a comparison between CMD/BOMD results and experimental data [9, 10, 29], we demonstrate the superior ability of BOMD to provide a quantitative description of the vanado-phosphate glass atomic structure, by improving upon previous conclusions drawn via CMD. Additionally, the use of BOMD allows gaining fundamental insights into the bonding and electronic properties of these systems.

Our paper is organized as follows. Section 2 reports on the CMD and BOMD methodologies and the model systems employed. The results are presented in four distinct sections, each one devoted to a specific set of properties. In Sec. 3 we provide a critical appraisal of the different V sites speciation when using CMD and BOMD schemes. Sec. 4 is devoted to the quantitative comparison between theory and experiments for the total structure factor S(k) and the pair correlation functions g(r). Also, the partial structure factors are analyzed in detail with a specific focus on the different pair interactions P−O, V−O, O−O. In Sec. 5 we consider the coordination numbers and the structural units found in the disordered network, together with the bond angle distributions and the bond order parameters. The analysis of chemical bonding and electronic properties can be found in Sec. 6. Section 7 reports a critical summary and discussion of the results, while some conclusions are drawn in Sec. 8.

2. Calculation methodology and models

2.1. Classical molecular dynamics

We employed the interatomic force field (FF) developed by Pedone et al. (named PMMCS) [33] in its recent upgraded version (named BMP-harm) [34], together with the potential parameters for V^{5+} and V^{4+} developed by Ori et al. [20]. The initial pairwise interatomic potential PMMCS was chosen because of its reliability and the availability of parameters for many cation-oxygen pairs [35]. Also, its ability to predict the mechanical properties has been well assessed for oxide glasses and oxide nanoparticles [36]. The revised BMP-harm version allows reproducing better the Si–O–Si and P–O–P bond angle distributions (BADs) and the oxygen-oxygen distances of the network former. In our CMD simulations, the short-range interactions were truncated at a distance of 10 Å, whereas the long-range interactions were calculated using the Ewald summation method with a precision of 10^{-5} eV, up to a cutoff distance of 13 Å. To ensure statistical significance, four replicas were generated, each consisting of 218 atoms (with a V^{4+}/V^{tot} ratio of 0.375), placed in a cubic box with dimensions adjusted to match the experimental density value of 2.8 g/cm^3 [9]. CMD simulations were performed using the DL-POLY code version 4.10.0 [37]. The Verlet leapfrog algorithm was employed with a time step of 1 fs to integrate the equation of motion. The VP50 glass models were obtained by melt-quenching thermal cycles following a well established computational strategy [20, 21, 33, 34]. The temperature control was implemented via the Nosé-Hoover thermostat [38–40]. First, the initial structures were randomly generated and relaxed at 300 K in the canonical (NVT) ensemble. Each system was heated to 5000 K and kept for 100 ps at this temperature. Then, cooling took place from 5000 K to 300 K with a cooling rate

of 2.5 K/ps, close to typical rates used within CMD for this type of glasses [20, 21, 33, 34]. Averages of relevant properties are taken on a structure obtained from the last 200 ps of a trajectory lasting for 500 ps at T= 300 K.

2.2. Born-Oppenheimer molecular dynamics

First-principles molecular dynamics simulations were carried out employing the Born-Oppenheimer approach as implemented in the CP2K package [41]. In such scheme, atom-centered Gaussian-type basis functions are used to describe the orbitals and an auxiliary plane-wave basis set is employed to re-expand the electron density. We employed double-ζ polarized MOLOPT basis sets [42] for V, P, and O, and used a cutoff energy of 800 Ry for the plane waves at the Γ point only. Goedecker–Teter–Hutter pseudopotentials were used to describe core-valence interactions [43] together with the semilocal Perdew-Burke-Ernzerhof (PBE) [44] exchange–correlation functional within a spin unrestricted density functional theory (DFT) formalism. The ionic temperature was controlled by a Nosé-Hoover thermostat [38–40]. Initially, four BOMD simulations equilibrated at T = 300 K during 5 ps were performed starting from an equal number of initially uncorrelated configurations sampled from the corresponding CMD trajectories. Then, we performed a final optimization at 300 K (~0.5 ps) of the electronic structure employing the hybrid functional PBE0 [45], in which 25 % of PBE exchange is replaced by nonlocal Hartree-Fock exchange, with a cutoff energy of 600 Ry [46, 47]. This final step allows a more accurate description of the electronic structure and spin topology [48]. The final 3 ps of the trajectory of each replica computed at the PBE level combined with 0.5 ps at the PBE0 level at T = 300 K were used to describe the structural properties of the VP50 model.

Analysis of the electronic structure and bonding properties was performed in terms of electronic density of states and the maximally localized Wannier functions (MLWF) [49, 50]. Following the standard procedure, the n^{th} MLWF $w_n(\mathbf{r})$ and the corresponding center $\mathbf{r}_n^{\mathrm{WFC}} = (x_n, y_n, z_n)$ are obtained as unitary transformation (iterative) of the Kohn-Sham orbitals $\psi_i(\mathbf{r})$

$$w_n(\mathbf{r}) = \sum_{i=1}^{N_{occ}} \left\{ \prod_p e^{-A_{i,n}^p} \psi_i(\mathbf{r}) \right\} \tag{1}$$

where N_{occ} is the total number of occupied states (i.e. electrons, in a spin-unrestricted approach), $A_{i,n}^p$ is a matrix generalization of the Berry phase connector, and p is the order of the iteration [51]. Among all the possible (equivalent) unitary transformations, in the case of MLWF we chose the one that minimized the spread of the orbitals. This is obtained by minimizing the spread functional Ω. This quantity represents the spatial extension of the Wannier orbital:

$$\Omega = \sum_{i=1}^{N_{occ}} \left\{ \langle i|r^2|i\rangle - \langle i|\mathbf{r}|i\rangle^2 \right\} \tag{2}$$

The Wannier function centers (WFC) of each Wannier orbital n are given by:

$$x_n = -\frac{L_x}{2\pi} Im \ln \langle w_n | e^{-\frac{i2\pi\, x}{L_x}} | w_n \rangle \tag{3}$$

where L_x corresponds to the length of the simulation cell along x. Similar equations are used for the coordinates along y and z. Being based on the correlation between atomic positions and the Wannier centers, the above framework allows gaining insight into the chemical bonding as shown for a wealth of systems such as liquid water [52, 53] and amorphous networks as TeO_2 [54], $Ge_2Sb_2Te_5$ [55], and GeS_2 [56]. In the present work, we calculated at the PBE0 level, WFC over 24 configurations sampled over the four BOMD models along the last ~3.5 ps of dynamics. All the structural results presented here were averaged every 0.35 ps over the four trajectories and from which the statistical uncertainty was determined.

3. Sites speciation in VP50 glass: the case of Vanadium

Vanadium, as a transition element, exhibits varying speciation (oxidation and coordination) in glasses [18, 57, 58], with oxidation states of V sites impacted by factors such as synthesis conditions, bulk chemistry, and total V amount. This results in the stabilization of V^{5+}, V^{4+}, and V^{3+} oxidation states, each with a unique local bonding environment [18, 19, 29, 57]. V^{5+} and V^{4+} states are the most commonly observed, as the highly reducing environment required for stabilizing V^{3+} is often difficult to achieve. From atomic-scale calculations standpoint, classical MD use predefined indexing to represent V sites in glasses, with V atoms in different oxidation states being labelled according to corresponding force field parameters. In contrast, BOMD simulations like all DFT approaches do not require a priori indexing of V sites, as the final V speciation is determined solely by the number of total oxygen atoms, corresponding to a defined $x V_2O_5$-$y VO_2$-$z P_2O_5$ composition. Various electronic charge determination methods,

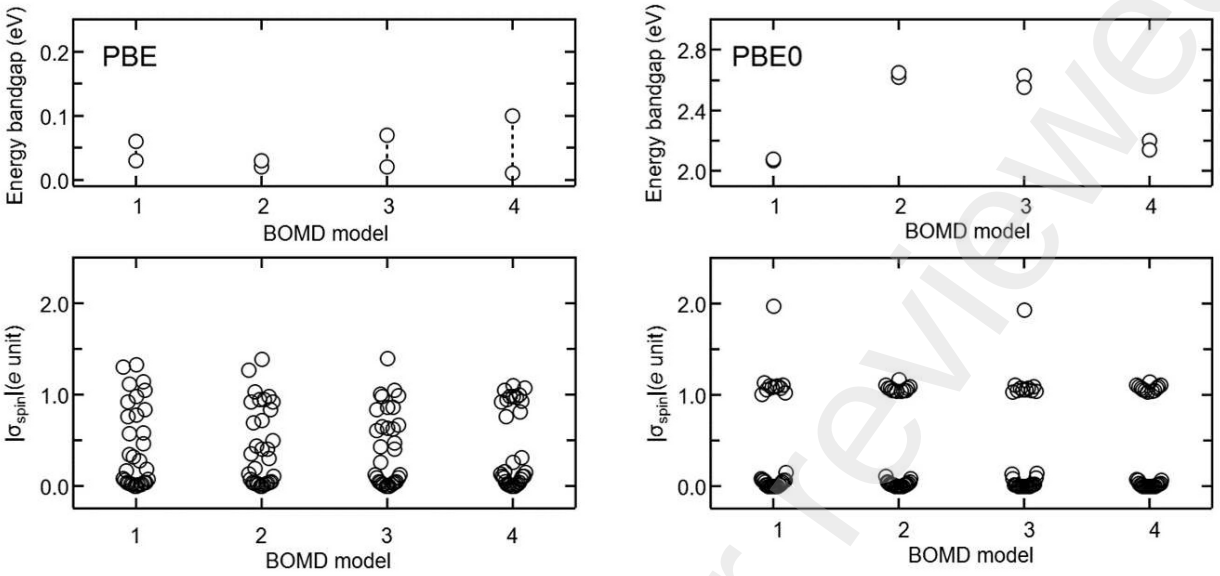

Figure 1: Values of energy bandgap (top, in eV) and spin densities σ_{spin} (bottom, in e units) computed for each V site at the PBE (left) and PBE0 (right) levels for the four individual BOMD models. Note that the bandgap values for both spin-up and spin-down states are reported for each of the four BOMD model implemented.

including Mulliken [59], Bader [60], and Qeq [61], have been tested to obtain information on vanadium speciation as post-processing of the configurations sampled from the BOMD trajectory. However, none of them was able to distinguish between different vanadium sites. To overcome this limitation and achieve proper identification of V speciation, we used local spin density projections of V sites associated with the calculation of energy bandgaps, as illustrated in Figure 1. For this purpose, we used both the PBE and the hybrid PBE0 functionals. PBE0 is expected to be more accurate giving an energy bandgap of about ~2.38 eV and ~2.35 eV for spin-up and spin-down states, respectively. In contrast, PBE functional resulted in very small bandgaps of approximately ~0.06 eV and ~0.04 eV (all values being obtained by averaging over four models). It is worth noting that even at the PBE level, we still observed a splitting of spin densities for model 4, which showed a finite bandgap of approximately 0.1 eV. The difference in energy between spin-up and spin-down states accounts for the non-negligible magnetic character of the VP50 glass, which can be associated to the possible presence of V^{4+} and V^{3+} sites. At the PBE0 level, our analysis revealed that the V sites exhibit local spin densities in a well-defined range values around 1.95 ± 0.03, 1.07 ± 0.03, and 0.02 ± 0.02 whereas all P and O atoms show values < 0.05. The values for V sites are indicative of the oxidation states of V^{3+}, V^{4+}, and V^{5+}, respectively, which correspond to the electronic configurations $3s^2 3p^6 3d^2$, $3s^2 3p^6 3d^1$ and $3s^2 3p^6 3d^0$. This finding is consistent with the magnetic character of V^{3+}, V^{4+}, and non-magnetic character of V^{5+} sites. V sites can be assigned in percentage to V^{3+} (0.8 %), V^{4+} (35.9 %), and V^{5+} (63.3 %) sites, in excellent agreement with the experimental determination by Hoppe *et al.* [9] (35.2 % for V^{4+} and 64.8 % for V^{5+} with a negligible content of V^{3+}). Based on these values, our calculations point toward a chemical composition corresponding to $32V_2O_5$-$18VO_2$-$50P_2O_5$ (without considering the negligible content, 0.4 %, of the V_2O_3 found). This is in contrast with the commonly assumed composition $50V_2O_5$-$50P_2O_5$, typically reported in the literature [9, 62].

4. Structural properties: structure factors and pair correlation functions

4.1. Total X-rays and neutron structure factors

In general terms, by considering an equilibrium trajectory, the structure factors (total structure factor, $S(K)$, or partial structure factors, $S_{\alpha\beta}(k)$) can be directly calculated in reciprocal space [63] or as Fourier transform (FT) of the real space corresponding pair correlation functions $g_{tot}(r)$ and $g_{\alpha\beta}(r)$. In both cases, one needs to keep track of the atomic coordinates, not necessarily at each time step (typically with a storage periodicity in

between 10^{-14}-10^{-15} s to describe accurately all vibration frequencies inherent in the system). Accordingly, for the so-called Faber-Ziman partial structure factors [64] the following relationships hold:

$$S_{\alpha\beta}(k) = 1 + \frac{1+\delta_{\alpha\beta}}{2N}\sum_{i}^{N_\alpha}\sum_{j\neq i}^{N_\beta}\left\langle \exp\left[-\mathbf{k}\cdot(\mathbf{r}_{i\alpha}-\mathbf{r}_{j\beta})\right]\right\rangle$$
$$= 1 + 4\pi\rho\int_0^\infty r^2\left[g_{\alpha\beta}(r)-1\right]\frac{\sin(kr)}{kr}dr, \quad (4)$$

with $\delta_{\alpha\beta} = 1$ if $\alpha = \beta$ and $\delta_{\alpha\beta} = 0$ if $\alpha \neq \beta$. $g_{\alpha\beta}(r)$ are the partial pair-correlation functions (for more detail on how to obtain the structure factors and the pair correlation functions within molecular dynamics, see [63, 65]). Having established that one can have access to the partial structure factors from an equilibrium trajectory (and in the absence of experimental information on these quantities) the total structure factors (X-ray or neutron) are readily obtainable. The total X-rays structure factor $S^X(k)$ is defined by:

$$S^X(k) = 1 + \frac{1}{|\langle f(k)\rangle|^2}\sum_{\alpha\beta} c_\alpha c_\beta f_\alpha(k) f_\beta^*(k)\left[S_{\alpha\beta}(k)-1\right] \quad (5)$$

where α and β refer to chemical species (P, V or O in the case of the present work), c_α is the atomic concentration of species α, ρ is the atomic number density equal to N/V (N, total number of atoms, V volume of the system), $f_\alpha(k)$ and $f_\alpha^*(k)$ are atomic form factor for the chemical specie α and its complex conjugate respectively and $\langle f(k)\rangle = \sum_\alpha c_\alpha f_\alpha(k)$ is the mean atomic form factor [63, 65].

In the case of the total neutron structure factor $S^N(k)$, $\langle f(k)\rangle$ in equation 5 is replaced by the mean coherent scattering length $\langle b\rangle = \sum_\alpha c_\alpha b_\alpha$ such that:

$$S^N(k) = 1 + \frac{1}{|\langle b\rangle|^2}\sum_{\alpha\beta} c_\alpha c_\beta b_\alpha b_\beta\left[S_{\alpha\beta}(k)-1\right] \quad (6)$$

Figure 2 shows the total structure factors, $S^X(k)$ and $S^N(k)$, obtained by CMD and BOMD simulations of the VP50 system. Our data are compared to the experimental results by Hoppe et al. [9]. We used the neutron scattering lengths and X-ray form factors reported in Table 1.

Concerning $S^N(k)$, we obtain a good agreement with the experimental results when considering peak positions and intensities for k values ≥ 3 Å^{-1}. However, both calculated neutron and X-ray structure factors overestimate the intensity of the first peak, located at ~2 Å^{-1}

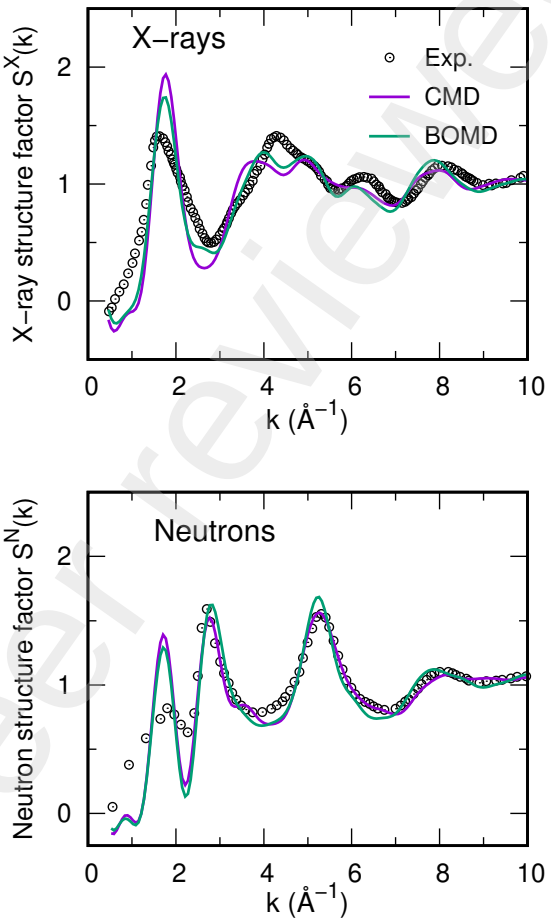

Figure 2: Total X-ray (top) and neutron (bottom) structure factors for VP50 glass simulated by CMD (purple line) and BOMD (green line) obtained through Fourier transform (FT) of the pair correlation functions. We also report the experimental data [9].

Table 1: Neutron scattering lengths b and X-ray atomic form factors f of V, P and O calculated at k=0 and for incident photon energy of 121.9 keV [66, 67].

Element	b (fm)	f (e/atom)
V	-0.382	23.022
P	5.131	15.005
O	5.803	8.000

. Furthermore, $S^X(k)$ is less performing at high k. This can be attributed to the fact that X-ray are more sensitive to the vanadium atomic environment due to the comparatively smaller vanadium neutron scattering length (-0.382 fm). The variety of local V coordination featuring multiple oxidation states leads to less structured $S^X(k)$ peaks compared to $S^N(k)$.

The agreement between theory and experiments is quantified by calculating the R_χ factor [68] defined by the equation (7)

$$R_\chi = \left(\frac{\sum_i \left[S^{exp}(k_i) - S^{sim}(k_i) \right]^2}{\sum_i \left[S^{exp}(k_i) \right]^2} \right)^{1/2} \quad (7)$$

In this formula, $S^{exp}(k_i)$ and $S^{sim}(k_i)$ refer to the experimental and the calculated structure factors at a given wave vector k_i. When the entire range of k values is considered, R_χ obtained via BOMD calculations is equal to 9.8 and 12.0 for the X-ray and neutron respectively. The corresponding values for CMD are 12.8 and 11.5 as shown in Table 2. This means that BOMD improves upon CMD quite when the total X-ray structure factor is considered as a whole, while the overall performance of the two methodologies is similar in the case of neutrons. By deferring any further analysis of this point to more detailed comparisons available in the next sections, we can also point out that, as expected, R_χ is quite high at low k for both CMD and BOMD simulations (arbitrary upper limit of integration $k \leq 2.8$ Å^{-1} for X-ray and $k \leq 4$ Å^{-1} for neutron), due to the strong overestimate of the first peak intensity. However, the significant reduction obtained when adopting BOMD instead of CMD in the X-rays case (15.4 against 20.3) is indicative of a drastic improvement in describing the local environment of V sites in VP50. Along the same lines, the comparable R_χ values obtained for neutrons (19.1 for BOMD, 18.5 for CMD) demonstrate the effectiveness of the force field potential in describing both O and P environments.

Table 2: Goodness-of-fit R_N and R_X parameters obtained from CMD and BOMD data indicating the level of agreement with the experimental data for neutron and X-ray structure factors respectively. All calculated values presented here are averaged over four parallel runs.

	CMD	BOMD
X-Rays		
$R^X_{S(k)}$	**12.8 ± 0.1**	**9.8 ± 0.1**
Neutrons		
$R^n_{S(k)}$	**11.5 ± 0.1**	**12.0 ± 0.0**

4.2. Total pair correlation functions

Here we introduce the notion of total correlation function $T(r)$ and its relationship with the total pair correlation function $g_{tot}(r)$ commonly employed to identify short-range structural features in a disordered solid. By referring to the case of neutron diffraction measurements, these two quantities are related by the following equation :

$$\begin{aligned} T(r) &= 4\pi\rho r + \frac{4\pi\rho r}{|\langle b \rangle|^2} \sum_{\alpha\beta} c_\alpha c_\beta b_\alpha b_\beta \left[g_{\alpha\beta}(r) - 1 \right] \\ &= 4\pi\rho r g_{tot}(r), \end{aligned} \quad (8)$$

A similar expression holds for the X-ray case provided the form factors take the place of the coherent scattering lengths. $T(r)$ can be also obtained by Fourier transform of the total structure factor through the following equation, in which $S(k)$ is a generic total structure factor obtained, as in the case of the experiments considered in this work, by X-ray or neutron measurements [9, 63].

$$T(r) = 4\pi\rho r + \frac{2}{\pi} \int_0^{k_{max}} dr\, k\, (S(k) - 1)\, M(k) \sin(kr), \quad (9)$$

where $M(k)$ is a modification function used to truncate $S(k)$ with $M(k) = 1$ for k ≤ k_{max} and $M(k) = 0$ for k > k_{max}.

Table 3: Goodness-of-fit R_N and R_X parameters obtained from CMD and BOMD data indicating the level of agreement with the experimental data for neutron and X-ray total correlation functions, respectively. All calculated values presented here are averaged over four parallel runs.

r range [Å]	CMD	BOMD
X-Rays		
$R^{X_1}_{T(r)}$ [1.32 - 2.20]	56.5 ± 0.4	33.7 ± 0.2
$R^X_{T(r)}$ [1.32 - 4.00]	**45.0 ± 0.2**	**32.0 ± 0.2**
Neutrons		
$R^{N_1}_{T(r)}$ [1.32 - 1.70]	59.0 ± 0.7	39.3 ± 0.8
$R^N_{T(r)}$ [1.32-3.2]	**37.9 ± 0.4**	**31.0 ± 0.4**

The total correlation functions obtained via CMD and BOMD systems are shown in Figure 3 (equation 8), together with the experimental data [9] (equation 9). BOMD results improves upon CMD on the intensity of the first peak for both X-ray and neutron total correlation function, as exemplified by the R_χ parameter values in Table 3 for two different ranges of distances. This is an unambiguous sign of the enhanced quantitative character of the BOMD approach when compared to CMD.

4.3. Partial pair correlation functions

CMD and BOMD partial pair correlation functions $g_{\alpha\beta}(r)$ are shown in Figure 4. In what follows, $g_{\alpha\beta}(r)$ calculated via the CMD or the BOMD approach will

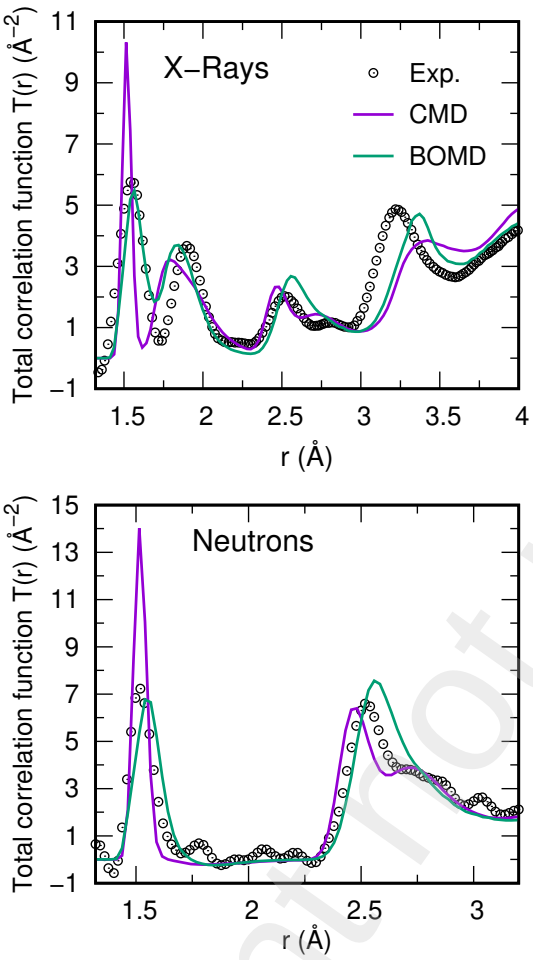

Figure 3: Total pair correlation functions for amorphous VP50 glass obtained at 300 K, by CMD (purple line) and BOMD (green line). The calculated results are compared to the experimental data from [9].

be also referred to as $g_{\alpha\beta}(r)$(CMD) and $g_{\alpha\beta}(r)$(BOMD), respectively. Bond distances are taken to correspond to the position of the first maximum of $g_{\alpha\beta}(r)$, allowing a comparison with experimental values, as reported in Table 4.

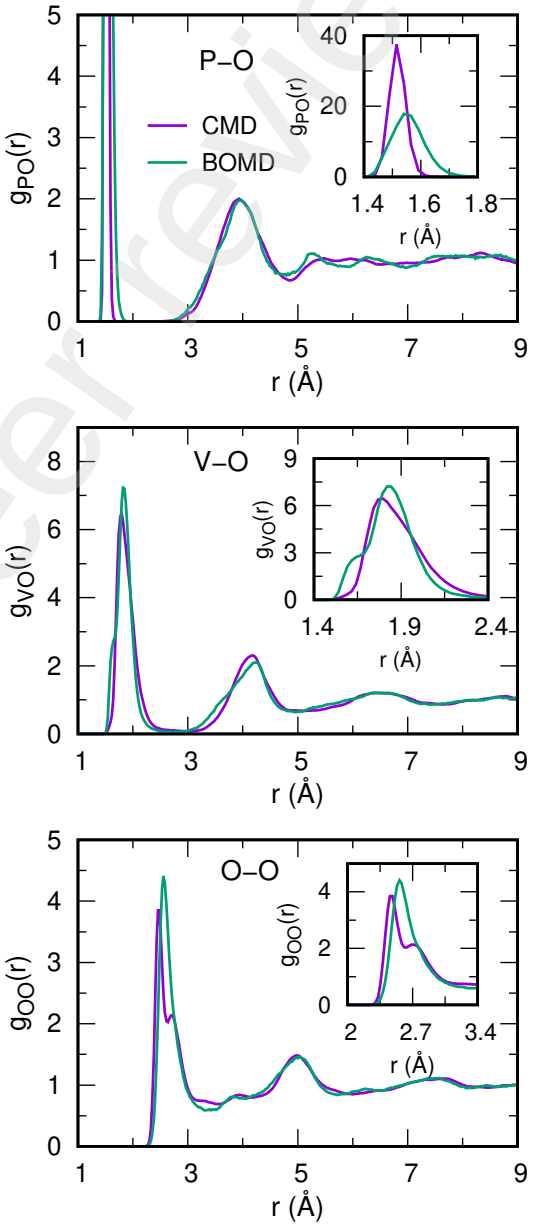

Figure 4: (Colors online) Partial pair correlation functions for the VP50 glass obtained at T = 300 K. From top to bottom: $g_{PO}(r)$, $g_{VO}(r)$, and $g_{OO}(r)$. Green lines refer to BOMD results and purple lines to CMD results.

***P–O pair*:** The first peak of $g_{PO}(r)$ is due to the four

P–O bond distances of PO_4 tetrahedral units. These units are composed of longer P–O bonds that connect P with three bridging oxygen (BO, two-folded O) atoms and one shorter P–O bond. This bond connects P to one nonbridging oxygen (NBO, one-folded O) atom. NBO bonds are associated with double P=O bonds, characterized by shorter bond lengths. Looking at Fig. 4 (top part), it appears that CMD and BOMD results have in common a sharp first peak centered at 1.51 Å and 1.55 Å, respectively. However, the first peak in $g_{PO}(r)$(CMD) is sharper and much more intense (see inset of Fig. 4, top part), accounting for the significant disagreement with the experimental counterpart. On the contrary, $g_{PO}(r)$(BOMD) provides a much better description of the bond distances of PO_4 units, with a first peak intensity close to experiments. P−NBO and P−BO bond distances obtained by CMD are found very close, being equal to 1.50 Å and 1.52 Å respectively. This can be interpreted as a shortcoming of the PMMCS/BMP force field since measurements have revealed a well-defined difference in bond lengths between the short double P=O bond and the longer single P–O bond, with values of 1.52 Å and 1.60 Å respectively [9]. It is worth noting that this was not the case for glasses containing alkali or earth ions, such as Na and Ca since the PMMCS/BMP force field was able to accurately capture the difference in bond lengths between P–NBO and P–BO bonds, with values equal to 1.47 Å and 1.58 Å, respectively, in agreement with experimental data [34]. In the present case, our deconvolution fitting of $g_{PO}(r)$(BOMD) (Figure 5) leads to bond lengths equal to 1.50 Å and 1.56 Å for the P=O and P–O bonds, respectively, in much better agreement with experiments. Therefore, it appears that CMD used with the PMMCS/BMP force field are somewhat suitable for modeling glasses containing alkali ions. However, they become inadequate in alkali ions-free vanadophosphate glasses, calling for a more quantitative approach such as BOMD to describe bonding in PO_4 units.

***V–O pair*:** The first peak of $g_{VO}(r)$ is due to the bond distances between O and V atoms in distinct VO_n structural units, which result from the different oxidation states of V. The picture of V−O bonding arising from $g_{VO}(r)$ differs when comparing CMD and BOMD descriptions. Specifically, $g_{VO}(r)$(CMD) exhibits an asymmetrical peak centered at 1.79 Å, while $g_{VO}(r)$(BOMD) features a peak with a maximum at 1.84 Å that is preceded by a clear shoulder. To better understand the scenario of bond distances in VO_n polyhedra, we show the breakdown of $g_{VO}(r)$ for the V sites with different oxidation states for both CMD and BOMD data in Figure 7. The asymmetrical profile of $g_{VO}(r)$(CMD) is found to be primarily due to the different peak positions and intensities of V–O bonds promoted by V^{5+} and V^{4+}, which are centered at 1.90 Å and 1.78 Å, respectively. A different situation is observed in $g_{VO}(r)$(BOMD), with $g_{V^{5+}O}(r)$ exhibiting a peak with maximal intensity at 1.81 Å that is preceded by a shoulder centered at 1.62 Å. In contrast, $g_{V^{4+}O}(r)$ has a small peak at 1.61 Å, followed by a more intense one centered at 1.87 Å. We also included $g_{V^{3+}O}(r)$ for completeness, although BOMD calculations revealed only a minor content of V^{3+}.

BOMD results are highly consistent with experimental data, since they capture the short vanadyl (double) bond V=O and longer single V–O bonds. These bonds lie in the range 1.55–1.75 Å and 1.83–2.31 Å, respectively. A notable feature reported in the literature for vanadophosphate crystalline phases is the increase of the length of V–O single bonds with decreasing V oxidation state. Also, V^{5+} and V^{4+} exhibit at least one vanadyl bond, while V^{3+} does not show any. For the VP50 glass, Hoppe *et al.*[9] reported multiple bonding distances for V^{tot}–O, including 1.58 Å, 1.90 Å, 2.10 Å, and 2.48 Å. Overall, BOMD calculations accurately describe the untrivial bonding pattern of VO_n polyhedra in good agreement with the reported experimental trends. In fact, one obtains short vanadyl and long single bonds of VO_n as well as an ordering of distances of single bonds with respect to the V oxidation state that goes as follows: V^{5+}–O<V^{4+}–O<V^{3+}–O (the respective values being 1.81 Å, 1.87 Å, and 1.95 Å). CMD results obtained via the PMMCS/BMP force field stand no comparison with the BOMD ones in reproducing the multiple bonding of VO_n polyhedra. The first peaks in $g_{V^{5+,4+}O}(r)$ are centered at distances between the vanadyl and single V–O bonds, with the V^{5+}–O bond length longer than the V^{4+}–O bond length, in clear disagreement with experimental data. However, it is worth noting that for a V oxide content relatively low, the PMMCS/BMP force field could accurately capture both short and long V–O bonds [20].

***O–O pair*:** The first peak of $g_{OO}(r)$(CMD) located at 2.47 Å is very sharp, followed by a less intense feature at 2.70 Å. Previous studies have indicated that the ratio of these two peaks depends on the glass composition [21]. In contrast, $g_{OO}(r)$(BOMD) has a positively-skewed peak with a maximum at around 2.56 Å. Further analysis through deconvolution peak fitting (Figure 5) reveals that the BOMD data can be fitted, minimizing the goodness-of-fit χ^2 parameter, with two peaks

Table 4: Bond lengths r_{ij} (in Å) (taken as the position of the first maximum of the pair correlation functions $g_{\alpha\beta}(r)$ and average coordination numbers n_i. For BOMD data, we report the distances obtained from the first maximum of $g_{\alpha\beta}(r)$ and its deconvoluted fitting (BOMD^g) together with the values obtained from the Wannier centers analysis (BOMD^w). We also report the experimental values for VP50 glass [69] and those found in crystalline vanadophosphate phases.

	Exp.	CMD	BOMD^g	BOMD^w
r_{PO}	1.52	1.50	1.50 ± 0.01	1.49 ± 0.02
	1.60	1.52	1.56 ± 0.01	1.60 ± 0.01
r_{VO}	1.58	1.79 ± 0.02	1.62 ± 0.02	1.67 ± 0.04
	1.90	-	1.84 ± 0.03	1.89 ± 0.06
$r_{V^{5+}O}$	1.59–1.78[a]	-	1.62 ± 0.02	1.65 ± 0.02
	1.80–2.35[a]	1.88 ± 0.02	1.81 ± 0.02	1.93 ± 0.05
$r_{V^{4+}O}$	1.59–1.74[a]	-	1.61 ± 0.02	1.74 ± 0.02
	1.80–2.12[a]	1.76 ± 0.02	1.87 ± 0.02	1.96 ± 0.04
$r_{V^{3+}O}$	-	-	1.68± 0.02	1.83 ± 0.03
	1.88–2.18[a]	-	1.95 ± 0.02	1.98 ± 0.05
r_{OO}	2.52	2.47 ± 0.01	2.54 ± 0.02	
	2.74	2.70 ± 0.03	2.72 ± 0.02	
r_{VV}	3.50	3.54 ± 0.01	3.50 ± 0.03	
r_{PV}	3.24	3.35 ± 0.01	3.35 ± 0.02	
n_P	3.9	4.00 ± 0.00	4.00 ± 0.00	
$n_{V^{tot}}$	5.4	5.09 ± 0.02	5.06 ± 0.01	
$n_{V^{5+}}$	-	5.38 ±0.02	4.81 ± 0.01	
$n_{V^{4+}}$	-	4.61 ± 0.04	5.53 ± 0.01	
$n_{V^{3+}}$	-	-	5.99 ± 0.01	
n_O	2.0–4.0[b]	1.89 ± 0.00	1.88 ± 0.01	

[a] Characteristic bond lengths intervals analysed from about 520 vanadophosphate crystalline phases [2, 30, 31].
[b] Mean coordination number interval of O atoms vanadium oxides and VP crystalline compounds reported by [9].

centered at 2.54 Å and 2.72 Å. The first peak is commonly associated with oxygen atoms in PO_4 tetrahedra units, which is a characteristic feature of other phosphate glasses [69]. The second peak at longer distances is attributed to oxygen atoms in corner-sharing VO_n structural units [9, 69, 70]. The distances obtained by both CMD and BOMD agree fairly well with experimental data reported by Hoppe *et al.*[9] for VP50 glass (2.52 Å and 2.74 Å).

5. Structural properties: atomic scale tools to describe the network

5.1. Coordination numbers and structural units identification

To gain further insights into the VP50 glass network, we can examine the averaged coordination numbers (n_i with i=P, O, V) by integrating the first peak of $g_{\alpha\beta}(r)$ up to a cutoff distance corresponding to the position of the first minimum. Figure 6 shows the running integrals of the individual partial correlation functions $g_{\alpha\beta}(r)$, from which we can extract the coordination numbers n_i, listed in Table 4, along with available experimental data. For V, we also report the contribution of individual oxidation states (V^{4+} and V^{5+} for CMD and V^{3+}, V^{4+}, and V^{5+} for BOMD).

As seen in Figure 6 and Table 4, CMD and BOMD lead to similar values for the average coordination of P, O, and total V, which are 4 (P), 1.9 (O), and 5.1 (V) in agreement with experiments. However, the breakdown of V coordination into different oxidation states highlights contrasting trends. The average n_V decreases (increases) with increasing (decreasing) V oxidation state for CMD and BOMD, respectively. While BOMD results agree with the experimental data, PMMCS/BMP force fields fail to properly describe the dependence of V coordination on the V oxidation state.
We also computed the distribution of the structural coordination units $n_\alpha(l)$ characterizing the environment of each atom. In this way, for a given number of neigh-

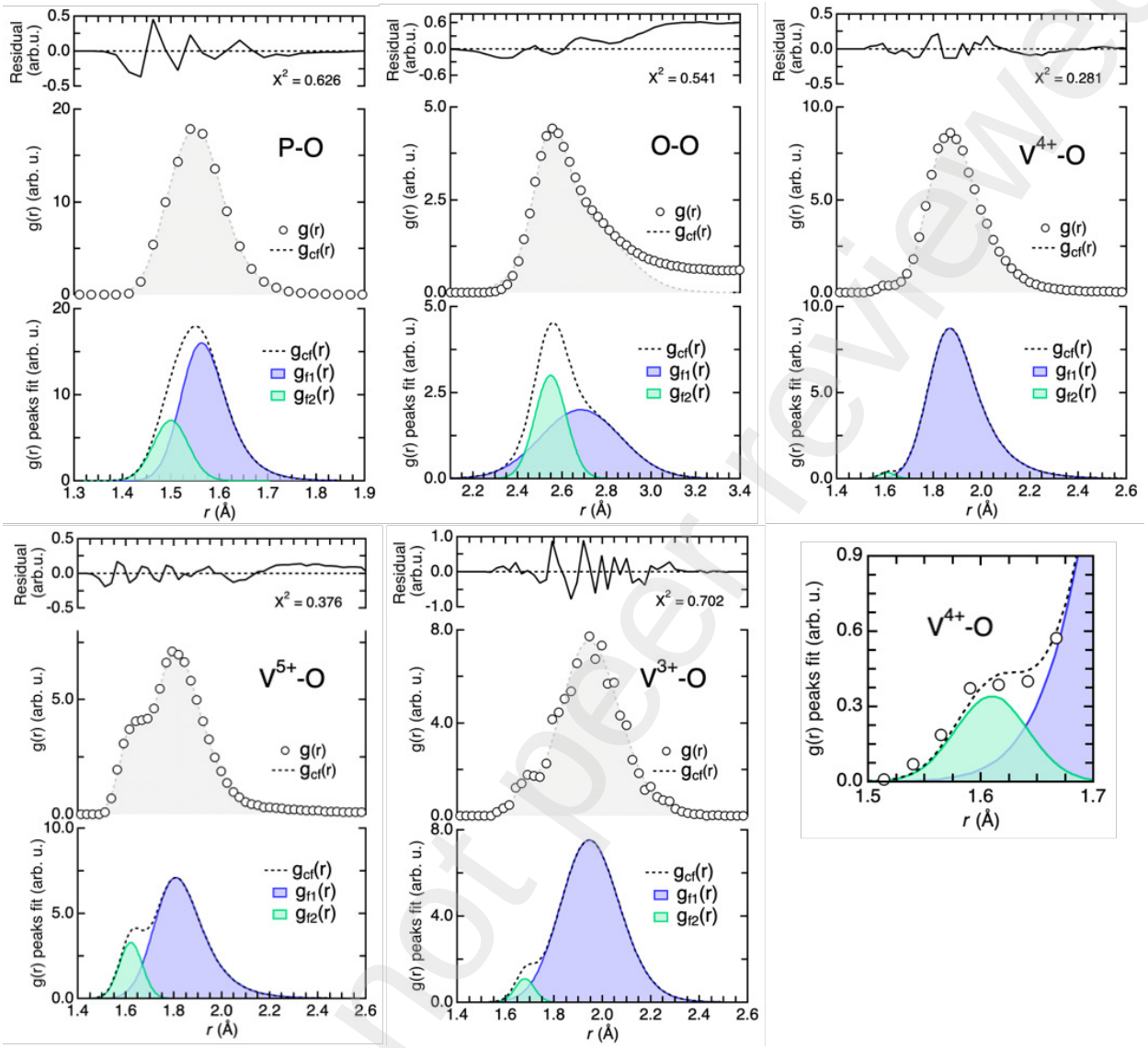

Figure 5: (Colors online) Deconvolution fitting of the P-O, O-O, V^{5+}-O, V^{4+}-O, and V^{3+}-O partial pair correlation functions simulated by BOMD. We report the calculated data ($g_(r)$, black circle), the cumulative fit ($g_{cf}(r)$, dashed gray line), the deconvolution fits of the peaks corresponding to the single and double bonds ($g_{f1,2}$(r), blue and green data) and the residual data. We give also the final X^2 as an indicator of the quality of the fit. For the V^{4+}-O partial pair correlation function, a zoom-in in the 1.5-1.7 Å interval is made available.

bors l and a given atomic species, one can extract from each configuration the chemical nature of the neighbors. It is important to underline the difference between n_i and $n_\alpha(l)$. The quantities n_i give an average behavior stemming from all neighbors with no insight into the detailed chemical nature of bonding, while the coordination structural units $n_\alpha(l)$ focuses on how each atomic species organizes itself when connecting to atoms of the same or of a different kind. The distributions of $n_\alpha(l)$ structural units for P, O, and V (V^{tot} and V^{3-5+}) are reported in Table 5, together with the breakdown of the chemical composition of each structural unit for a given l. The results indicate that the first coordination shell of P is entirely made of fourfold connections, as in PO_4 units, in agreement with experimental data. Regarding the first coordination shell of O atoms, CMD and BOMD results are similar. We found that ~88% of O atoms are two-folded, while ~12% are one-folded. The decomposition in terms of chemical species reveals that two-folded O atoms are mainly coordinated with

Table 5: (Colors online) Distribution of the individual $n_\alpha(l)$ structural units where an atom of species α (P, V or O) is l-fold coordinated. In bold are reported the total percentages determined for each l-fold coordination. These quantities have been calculated including neighbours separated by a cutoff corresponding to the first minimum in the $g_{\alpha\beta}(r)$. For the present work, the cutoffs of 2.0 and 2.4 Å was used for the P-O and V-O bonds respectively. The values with a star (*) correspond to the appearance of certain vanadium environment configurations in low concentrations. Only fraction greater than 0.5 % are reported.

		CMD	BOMD			CMD	BOMD
V^{tot}				V^{5+}			
$l=4$	O_4	**22.2 ± 1.4**	**26.9 ± 0.5**	$l=4$	O_4	4.8 ± 0.6	25.7 ± 0.5
$l=5$	O_5	**46.3 ± 1.2**	**40.4 ± 0.6**	$l=5$	O_5	28.9 ± 0.7	24.7 ± 0.4
$l=6$	O_6	**31.5 ± 0.7**	**32.0 ± 0.3**	$l=6$	O_6	28.8 ± 0.7	12.3 ± 0.5
P				V^{4+}			
$l=4$	O_4	**100.0 ± 0.0**	**99.3 ± 0.1**	$l=4$	O_4	17.4 ± 1.1	1.2 ± 0.2 *
O				$l=5$	O_5	17.4 ± 0.9	14.7 ± 0.6
$l=1$		**11.0 ± 0.5**	**12.1 ± 0.2**	$l=6$	O_6	2.8 ± 0.3	20.1 ± 0.5
	P	10.0 ± 0.4	9.1 ± 0.1	V^{3+}			
	V	1.0 ± 0.1	2.9 ± 0.1	$l=4$	O_4	-	-
$l=2$		**87.8 ± 0.5**	**87.6 ± 0.2**	$l=5$	O_5	-	-
	VP	71.6 ± 0.5	73.6 ± 0.1	$l=6$	O_6	-	0.8 ± 0.0*
	V_2	16.2 ± 0.1	13.9 ± 0.1				

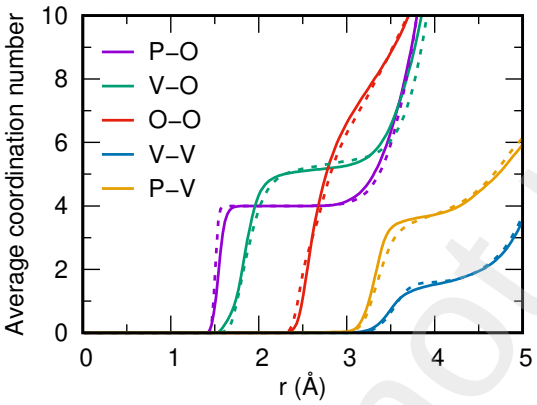

Figure 6: (Colors online) Running averaged coordination number for CMD (dashed line) and BOMD (solid line).

one P and one V (VP), with ~72% (CMD) and ~74% (BOMD). Additionally, O coordinated by two V atoms (V_2) accounts for ~16% (CMD) and ~14% (BOMD) of the coordination units. The percentage of O coordinated to only one V is slightly higher in BOMD (~3%) than in CMD (~1%).

The majority of V atoms are five-folded coordinated, resulting in ~46% (CMD) and ~40% (BOMD). Around ~32% of V atoms are six-folded coordinated in both CMD and BOMD simulations, while approximately ~22% (CMD) and ~27% (BOMD) of V is four-folded coordinated. Therefore, the environment of V is dominated by five- and six-folded coordinations, with four-folded coordination being the least abundant. An anal-

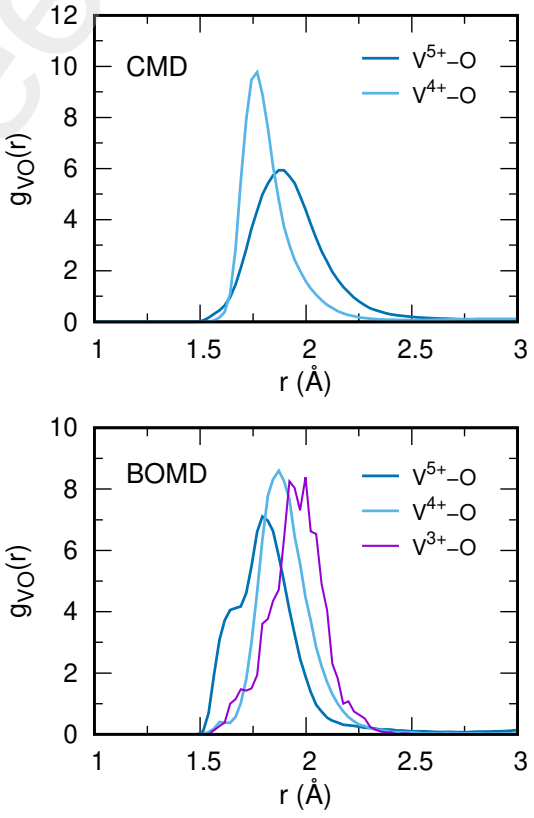

Figure 7: (Colors online) V-O partial pair correlation functions for different oxidation states of vanadium. Upper part: CMD results, lower part: BOMD results.

ysis of the breakdown of V units in terms of different V oxidation states reveals striking differences between CMD and BOMD. In the case of V^{5+}, CMD shows that five-folded (VO_5) and six-folded (VO_6) coordination units are equally distributed, accounting for ∼29% of the total V content, while four-folded (VO_4) units are less common, only ∼4%. Conversely, for V^{4+}, CMD calculations show an equal content (∼17%) of VO_4 and VO_5, and a minor content of VO_6 (∼3%). These results are found to be in strong disagreement with experimental data. Different conclusions can be drawn on the basis of BOMD calculations. For V^{5+}, VO_4 and VO_5 are present in very close percentages, ∼26% and ∼25%, while for VO_6 one has ∼12%. Notably, for V^{4+}, BOMD leads to the majority of V^{4+} found in VO_6 and VO_5 coordination units, accounting for approximately ∼20% and ∼15%, respectively, while the amount of four-fold VO_4 is found to be negligible (∼1%). The content of V^{3+} is negligible in the BOMD case, this motifs being found in VO_6 units, in accordance with experimental evidence.

5.2. *Bond angle distributions, local order parameter and network connectivity*

The bond angle distributions (BAD) of triads O-V-O, centered around V^{5+} and V^{4+} atoms are shown in Figure 8. For O–V^{5+}–O triads, CMD results show a prominent peak at around 90° and a second one at 170°, taken to correspond to (defective) octahedral and pyramidal units and defective square and trigonal pyramids, respectively. The O–V^{4+}–O CMD data exhibit a broad band between 85° and 120°, and a minor peak at 170°. In contrast, BOMD O–V^{5+}–O data are characterized by a first peak at around 90°, which corresponds to octahedral and pyramidal units, in addition to a secondary peak centered around 105°, attributed to the tetrahedral structure of $V^{5+}O_4$ units. There is also a less intense third peak centered at approximately 170° due to contributions from defective square and trigonal pyramids. For O–V^{4+}–O, BOMD features a prominent peak at 90°, which is typical of octahedral, pyramidal, and square pyramidal structures, and no contribution at around 109°, in agreement with the negligible quantity of $V^{4+}O_4$ connections found in this case. Finally, the second peak at 170° is slightly more intense than in the CMD case.

To further gain insights into the structural properties of VP50, we calculated the q parameter indicative of structural order,

$$q = 1 - \frac{3}{8} \sum_{j} \sum_{k \neq j} \left(\cos \theta_{jik} + \frac{1}{3} \right)^2, \qquad (10)$$

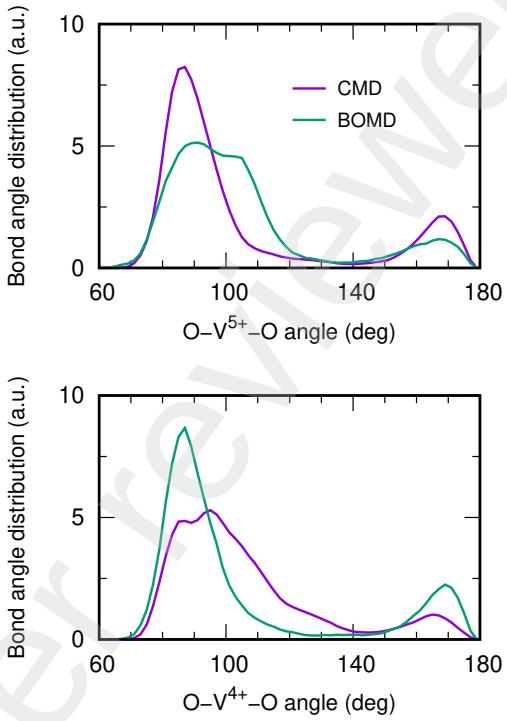

Figure 8: (Color online) from top to bottom O-V^{5+}-O and O-V^{4+}-O bond angle distributions obtained via CMD and BOMD at T = 300 K.

where θ_{jik} is the bond angle constructed from the central atom i and its neighbours j and k ($j, k \leq 6$). q varies is equal to 0 for perfect six-fold octahedral and to 1 for four-fold tetrahedral structure [71]. This parameter is a useful tool for identifying the individual contributions of different structural units to the overall structural order as proven for a variety of amorphous systems, including glassy chalcogenides [72], chalcohalides [73], and phase-change materials [55, 74]. The calculation of q for P sites in VP50 glass yielded a value near 1 for both CMD and BOMD simulations, which is indicative of the presence of P uniquely in tetrahedral PO_4 units, in a way consistent with experimental observations.

As shown by the analysis of the V sites, VO_5 and VO_6 are the dominant vanadium structural units, comprising 72% of the vanadium content in the BOMD case. Their corresponding q-parameter ranges in between 0.65 to 0.85, indicating the prevalence of distorted octahedra (VO_6) and defective square pyramids (VO_5), with a few trigonal bi-pyramidal units observed in VO_5. Notably, V^{5+} units form mostly tetrahedral connections similar to PO_4 with a q-value close to 1. Apart from tetrahedral polyhedra, the parameter q has limitations in quantitatively assessing the various VO_n polyhedra

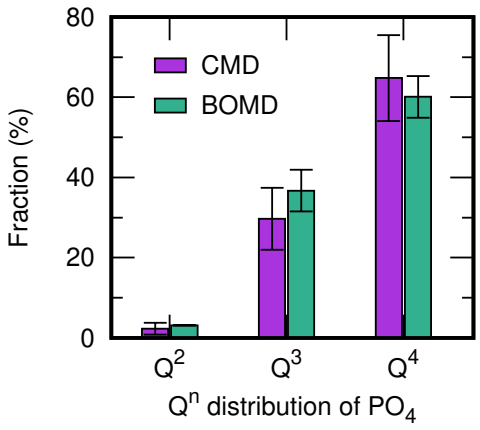

Figure 9: Q^n distribution (with n the number of bridging oxygen per polyhedra unit) of and PO_4 units in VP50 glass for CMD and BOMD calculations.

in the VP50 glass structure. This is due to the distorted nature of these polyhedra, resulting in varying q values even for polyhedra with the same geometric shape. These values deviate significantly from the reference ones [65].

Additional calculations were performed to obtain the Q^n species distribution, providing information on the degree of polymerization of the polyhedra into the three-dimensional network [28, 75]. Q^n is defined as a unit in which n bridging-oxygen (BO) atoms are directly linked to a network former ion, such as Si and P in silicate and phosphate glasses. Figure 9 shows the breakout of the Q^n distribution for P sites in PO_4 tetrahedral units, showing similar results for CMD and BOMD calculations and featuring a majority of Q^4 (~60%) and a non-negligible content of Q^3 (~37%). The amount of Q^2 is negligible (≤3%). These findings are in excellent agreement with the experimental data of Hoppe *et al.*[9] pointing to a coexistence of Q^4 and Q^3 units (note that in [9] the Q^n notation employed is different, with n denoting the number of non-bridging oxygen atoms). We further explored the Q^n distribution for the V sites in VP50 glass, and the analysis was organized into contributions from V^{5+}, V^{4+}, and V^{3+}, as illustrated for both CMD and BOMD in Figure 10. The CMD data reveals that the majority (~25%) of the local connectivity for V^{5+} is composed of Q^5 and Q^6 species, with only a small proportion of Q^4 and Q^3. Conversely, for V^{4+}, a similar proportion of Q^4 and Q^5 species (~17%) have been identified as the most abundant. The situation changes in the BOMD case. Q^4 (~25 %) is the most abundant

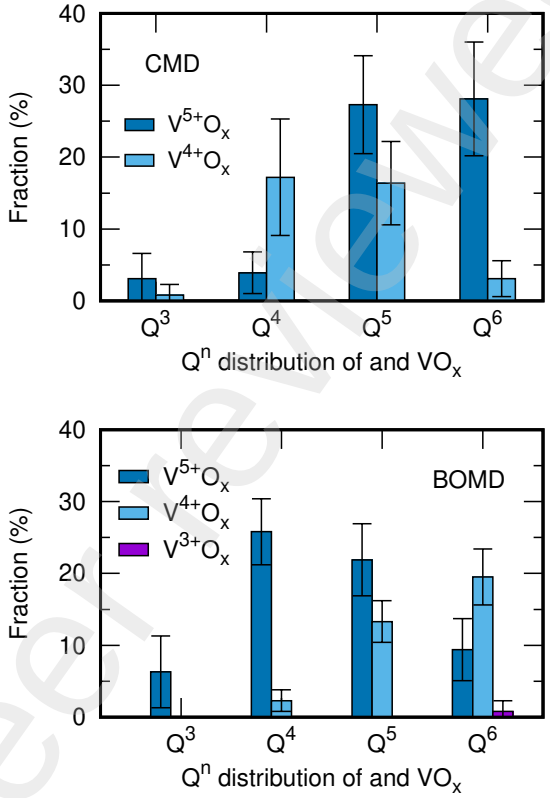

Figure 10: Q^n distribution (with n the number of bridging oxygen per polyhedra unit) of VO_x (for V^{5+}, V^{4+}, and V^{3+} oxidation states) units describing the network connectivity in glassy VP50.

unit for V^{5+}, followed by ~22 % of Q^5, ~9 % of Q^6, and ~6 % of Q^3. The most frequent Q^n units for V^{4+} are Q^5 and Q^6, accounting for ~13 % and ~20 % of the total occurrences, respectively. The few V^{3+} sites found with BOMD have been identified as Q^6. Overall, this analysis demonstrates that the VP50 glass is a highly polymerized disordered network.

6. Electronic and bonding properties

As a first piece of information, the electronic properties of glassy VP50 are investigated via the electronic density of states (EDOS) shown in Figure 1. To minimize the underestimate of the band gap inherent in DFT, we employed the hybrid functional PBE0 (intended to provide more realistic values due to inclusion of Hartree-Fock contributions) and obtained values of ~2.38 eV and ~2.35 eV for spin-up and spin-down states, respectively. This means that VP50 glass is a wide-bandgap semiconductor with a small and yet sizeable magnetic character as several crystalline

phases of $VOPO_4$ vanadyl phosphates, for which reported bandgap values are in between 2.5–2.9 eV [76]. To gain a deeper understanding of chemical bonding we resorted to the maximally localized Wannier function centers (WFC) by focusing mostly on the WFC proximal to O atoms, as O is the most electronegative element in VP50 and neither P or V contribute with any lone pair electrons. We considered the pair correlation function g_{O-W} obtained at the PBE0 level, shown in Figure 11 a). The partial pair correlation function $g_{O-W}(r)$ exhibits a distinct band ranging from 0.2–0.5 Å, characterized by three maxima. The more intense one is located at 0.29 Å, while the other two are centered at 0.40 Å and 0.47 Å. In what follows, we focus on the contributions of PO_4 and VO_n polyhedra to the peaks of $g_{O-W}(r)$.

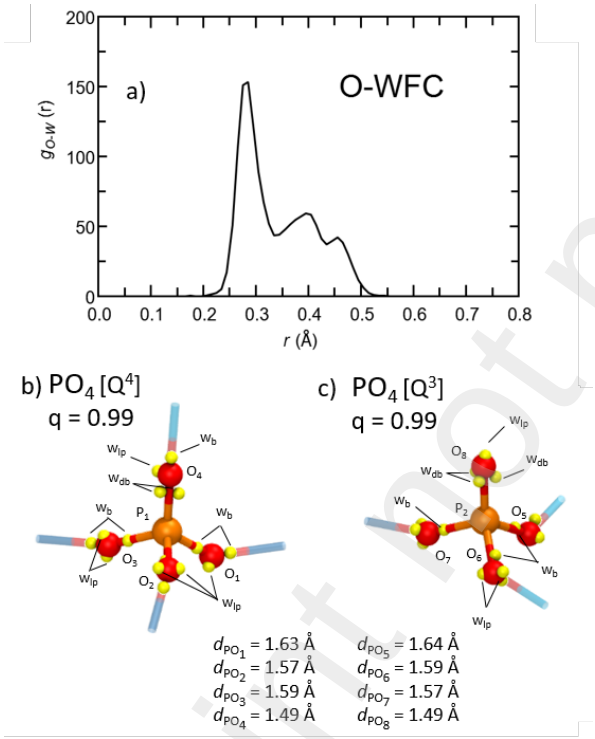

Figure 11: (Colors online) a) Partial pair correlation function g_{O-WFC}. b,c) Atomistic view of two tetrahedral PO_4 units found in VP50 glass by BOMD at 300 K. We show P and O atoms in orange and red respectively. P-O bonds are colored as orange-red. Their bond distances as well as the PO_4 order parameter values q are reported. The transparent red/blue bonds correspond to neighbouring V-O bonds. P_1 atom is surrounded by four V-O-P bridging oxygen atoms (Q^4) whereas P_2 atom is surrounded by three V-O-P bridging oxygen atoms and one non-bridging oxygen (Q^3). We also show the Wannier centers (yellow) involved in the local environment of each PO_4 unit, as in single bonds (w_b; P_1–$O_{1,2,3}$ and P_2–$O_{5,6,7}$), lone pairs (w_{lp}) and as centers involved in double P=O bonds (w_{db}; such as P_1–O_4 and P_2–O_8).

***P–O chemical bonding*:** Figure 11 (b) and (c) provides an atomistic view of two tetrahedral PO_4 units (with ∼109° $O\hat{P}O$ angles), observed via BOMD calculations at 300 K. The first is a tetrahedral Q^4 PO_4 unit (q= 0.99), composed of one P (P_1) bonded to four bridging oxygen atoms via P-O-V linkages. The second unit also comprises a tetrahedral Q^3 PO_4 unit (q= 0.99), consisting of one P (P_2) bonded to three bridging O atoms through P-O-V linkages and one non bridging O atom. The arrangement of WFC centers in the local atomic environment surrounding these units is representative of three different WFC types, to be correlated to distances identified by the three maxima of g_{O-WFC}. Specifically, we are referring to:

- i) WFC due to lone pair electrons (w_{lp}) having very short O-WFC distances (0.29 Å).
- ii) individual WFC (w_b) involved in single σ_{P-O} bonds (∼1.60 Å; e.g. P_1–O_{1-3} and P_2–O_{5-7} in Fig. 11 b)-c) and displaying a long O-WFC distance (0.48 Å).
- iii) double or triple WFC (w_{db}; P_1–O_4 and P_2–O_8 in Fig. 11b)-c) respectively) involved in short bonds (∼1.49 Å) and featuring an intermediate O-WFC distance (0.40 Å).

All bonding WFC are found closer to O atoms than to P atoms, denoting highly polarized iono-covalent P–O bonds with localized distribution of valence electron density closer to O sites [77]. The presence of two WFCs in the short bonds is consistent with the simple Lewis picture of double P=O bonding, while the presence of three WFC identifies mixed σ–π orbitals that give rise to so-called "banana bond" τ orbitals [78, 79]. We have observed that P=O and O-WFC distances remain the same regardless of the nature of the Wannier centers and the bridging or non-bridging character of oxygen atoms allowing us to identify these bonds as double P=O bonds. The WFC approach promoted a more precise scrutiny of P–O interatomic distances, thus substantiating the values previously determined through the analysis of g_{P-O}. Overall, all values obtained (see Tab. 4, ∼1.60 Å and ∼1.49 Å, respectively) are found in excellent agreement with the experimental data [9].

***V–O chemical bonding*:** The kind of $V^{5+}O_n$ units found in the VP50 glass are shown in Figure 12. These units are: a four-folded V^{5+} tetrahedral Q^3, a five-folded V^{5+} in square pyramidal or trigonal bi-pyramidal Q^5

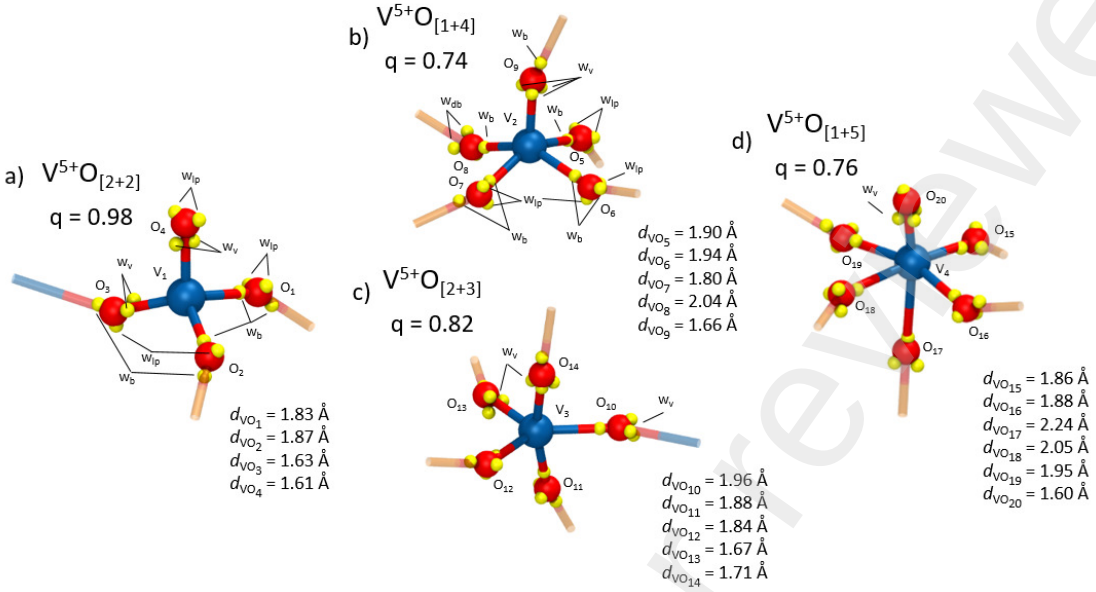

Figure 12: (Colors online) Snapshot of various $V^{5+}O_n$ polyhedra units within the VP50 glass network. The local atomic environment of V^{5+} sites is described by V^{5+}-O bond lengths and associated Wannier centers (highlighted in yellow). The polyhedra include: a) a tetrahedral unit standing for a VO_4 polyhedron with order parameter $q = 0.98$, b) a square pyramidal unit ($q = 0.74$), c) a defective trigonal bi-pyramidal unit ($q = 0.82$), and d) a distorted octahedral unit ($q = 0.76$)

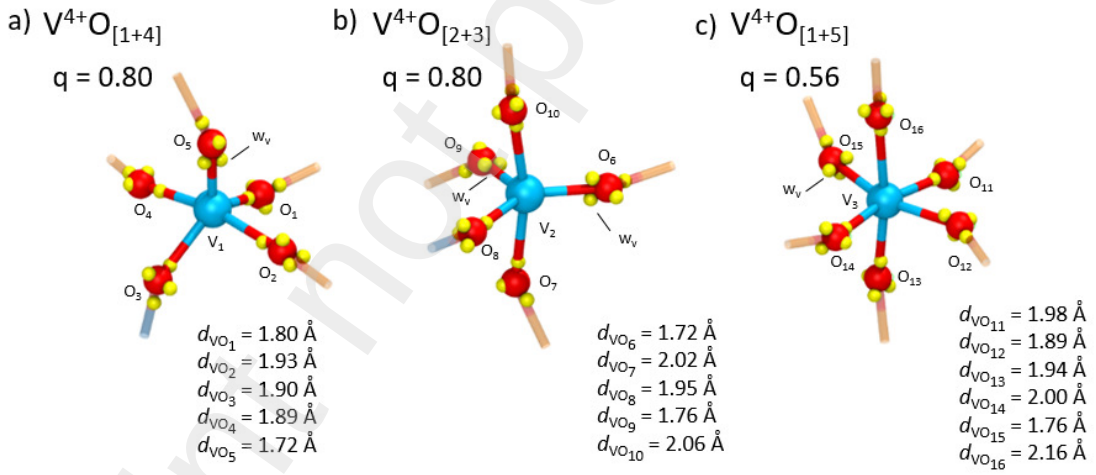

Figure 13: (Colors online) Snapshot of $V^{4+}O_n$ polyhedra units within the VP50 glass network. The local atomic environment of V^{4+} sites is described by the V^{4+}-O bond lengths and associated Wannier centers (highlighted in yellow). The polyhedra include: a) a defective square pyramidal unit with the local order parameter $q = 0.80$, b) a defective trigonal bi-pyramidal unit ($q = 0.80$), and c) a distorted octahedral unit ($q = 0.56$).

configuration, and a six-folded V^{5+} in a distorted octahedral Q^5 unit [30, 31]. The arrangement of WFC centers in the local atomic environment of these units correspond to three different WFC types. These are characterized by different O-WFC distances identified by the three maxima of g_{O-WFC}. One has:

- i) WFC representing lone pair electrons (w_{lp}) at very short O-WFC distances (0.29 Å)
- ii) individual WFC (w_b) involved in single $\sigma_{V^{5+}-O}$

bonds with O-WFC distance of 0.40 Å

- iii) double or triple WFC (such as V_1–$O_{3,4}$, V_2–O_9, V_3–$O_{13,14}$, and V_4–O_{20}) involved in short bonds (∼1.61–1.71 Å) with longer O-WFC distance (0.48 Å).

The analysis of chemical bonds and related distances based on the WFC approach enables us to classify any V–O interaction longer than ∼2.4 Å as a non-chemical bond. This is because the next closest O atom is associated to a WFC with w_{lp} characteristics.

All the bonding WFC found in the local atomic environment of V are in closer proximity of O atoms than V, prompting a description in terms of highly polarized iono-covalent bonds [77]. Furthermore, in the case of VO_n polyhedra, the finding of double or triple WFC in short bonds is consistent with the picture of double or τ bonds and are denoted as vanadyl bonds [2, 30, 31]. These WFC are referred to as w_v in Figure 12, allowing us to describe the coordination of VO_n within the formalism used in [9, 30, 31]. This consists in replacing the subscript n with two indexes, the first one being the number of vanadyl bonds and the second one the number of single bonds, the sum of the two being the total coordination of the V atom (i.e. $V^{5+}O_{[1+4]}$ identifies a $V^{5+}O_5$ unit with one vanadyl bond and four single bonds). The single and vanadyl bond distances obtained from the WFC analysis are reported in Table 4. They are in better agreement with the range of values reported in the experiments than those extracted from g_{V-O}. For instance, averaged V^{5+}–O single and vanadyl bonds are ∼1.93 Å and ∼1.65 Å, respectively.

Figure 13 exemplifies the typical $V^{4+}O_n$ units present in the VP50 glass, consisting of V^{4+} in a five-fold coordination, either in a square pyramidal arrangement ($V^{4+}O_{[1+4]}$) or a by-pyramidal arrangement ($V^{4+}O_{[2+3]}$), and in a six-fold coordination as a distorted octahedral unit ($V^{4+}O_{[1+5]}$) as well. $V^{4+}O_n$ polyhedra display the three types of distorted WFC centers, with average vanadyl and single bond distances of ∼1.74 Å and ∼1.96 Å, respectively. Once again, these results are in better agreement with the experimental data than the values obtained from $g_{V^{4+}O}(r)$. The contribution to $g_{V^{4+}O}(r)$ due to vanadyl bonds, which was quantified previously by deconvolution fitting of $g_{V^{4+}O}(r)$, was underestimated because of the presence of the whole $g_{V^{4+}O}(r)$ peak corresponding to single V–O bond distances (see Fig.13). Furthermore, the average value of single bonds increases slightly from $V^{4+}O_5$ to $V^{4+}O_6$ (∼1.95 Å and ∼1.99 Å).

Although the content of V^{3+} in the VP50 glass is found minimal, some details related to this unit are worth mentioning. Figure 14 illustrates the typical coordinating unit found in this case, namely a six-coordinated Q^6 $V^{3+}O_{[1+5]}$ unit in a distorted octahedral polyhedra. There is a relatively long single V–O bond distance of ∼1.98 Å, which is consistent with the range of values reported in literature. One double WFC localization along one of the V–O bonds becomes visible along a particularly elongated V–O bond (∼1.83 Å). This distance lies at the boundary between vanadyl and single bond values. However, vanadyl bonds have not been reported for V^{3+}-containing polyhedra in vanadophosphate crystalline phases. Therefore, we can legitimately label this bond as a weak vanadyl bond or a relatively short single V–O bond.

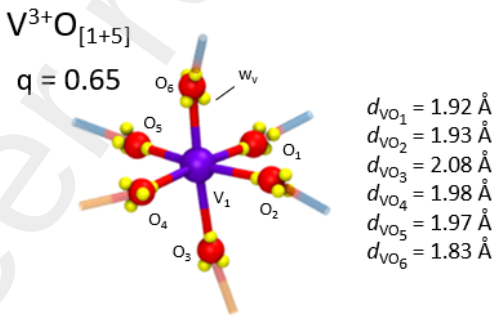

Figure 14: (Colors online) $V^{3+}O_n$ polyhedra unit the VP50 glass network. The local atomic environment of V^{3+} sites is described by the V^{3+}-O bond lengths and associated Wannier centers (highlighted in yellow). The polyhedra shows a distorted octahedral unit with local order parameter value of q = 0.65.

7. Discussion

7.1. General remarks

Classical molecular dynamics has been increasingly used for modeling VP glasses, by complementing the experimental findings and offering qualitative insights into their structural properties. However, a quantitative assessment of the structural properties as well as a precise understanding of electronic structure and bonding is still missing. In this section, we delve into the limitations of CMD in modeling VP glasses, and highlight the importance of incorporating electronic structure via FPMD (in this case within the BOMD framework) as we have done in the present work. One of the most significant advantages of using BOMD is its ability to determine the chemical speciation of V sites

in VP50 glass. BOMD allows defining the final composition of V oxidation states, which is found in excellent agreement with experimental data (BOMD: 0.8 % V^{3+}, 35.9 % V^{4+} and 63.3 % V^{5+} *versus* exp.: 35.2 % V^{4+} and 64.8 % V^{5+} [9]) without any a priori information but the total O content. This stands in stark contrast to classical force fields used in CMD, which require the indexing of the number of different V sites with distinct oxidation states and the development of parameters for each pair at the start. The accurate determination of V speciation by BOMD is shown to be critically reliant on the correct description of the electronic properties of the glass, requiring the use of hybrid exchange-correlation functional such as PBE0 to correct energy bandgap underestimation effects. The calculated bandgap (2.35–2.38 eV) allows us to define VP50 glass as a wide-bandgap semiconductor with a small but sizeable magnetic character.

7.2. Reviewing the atomic structure: short-range and intermediate-range order

The short-range order of glassy VP50 was analyzed using X-rays and neutron total structure factors in reciprocal space as well as the total correlation functions in real space through the use of CMD and BOMD approaches, which were compared to experimental data. BOMD captured the majority of the structural details observed in experiments, with a notable improvement over the performance of CMD. Notably, contributions from both the local atomic environment of the phosphate and vanadate polyhedra in the pair correlation functions were identified within the 1.5–2.4 Å interval of distances. The improvements observed in the BOMD description stem from the correct description of double bonds P(V)=O and single bonds P(V)–O. CMD fails to describe the short-range order of VP50 glass as shown by the very close values recorded for double P=O and single bond P–O bond distances, leading to overstructuring in the total correlation function at short distances. In terms of V–O bond distances, the failure of CMD is more pronounced, the splitting between the vanadyl double and single bonds being absent. Also, one cannot recover the correct single bond distance dependence on the V oxidation state. In this context, the analysis of bonding properties based on the Wannier functions centers has proved to be crucial to assess the variety and diversity of double and single V–O bonds.

As shown by experiments [9, 29–31], V^{5+} features three types of coordination in VP glasses and crystalline phases, including VO_4 (tetrahedral (T_h)), VO_5 (trigonal bi-pyramid (T_b) and square pyramid (S_p)), and VO_6 (distorted octahedra (O_d)). For V^{4+} one has VO_5 (S_p and T_b) and VO_6 (O_d) coordination, while V^{3+} can be found coordinated in regular octahedra (O_h) VO_6. Our BOMD calculations substantiated these experimental findings. For our VP50 system, the following summary of structural units can be compiled:

- V^{5+} is preferentially coordinated as four- and five-folded (~26 % and ~25 %, respectively), as T_h and S_p/T_b (with S_p as mostly present), and with a non-negligible content of six-folded V^{5+} (~12 % as O_d);
- V^{4+} is preferentially coordinated as six- and five-folded (~20 % and ~15 %, respectively), as O_d and S_p/T_b (with S_p as mostly present), and with negligible content of four-folded V^{4+} (~1 %);
- V^{3+} is preferentially coordinated as six-folded (O_d), although it has been found in negligible amount in VP50 glass (<1 %).

The CMD approach has a limited ability to describe the individual coordination with respect to the different V oxidation states. Notably, CMD fails to predict the presence of V^{4+} as a four-fold coordinated unit, which is inconsistent with experimental data.

The absence of any peak at wave vectors smaller than the main peak in the structure factors reveal that the intermediate range order (intended as a structural organization manifesting itself via a discernible feature at short wavelength in reciprocal space) is very limited or even absent in VP50 glass. In terms of hypothetical topological features extending on intermediate range distances, we observe that the analysis of the distribution of structural units in the VP50 glass is indicative of no discernible segregation of the phosphate (PO_4) units, which are well distributed throughout the glass matrix. This is shown by the absence of signatures indicating connections between the PO_4 units, with a negligible percentage of two-fold coordinated O atoms bound to two P atoms (≤0.1 %). There is also a limited segregation within the vanadate (VO_n) network, with approximately ~14 % of two-fold coordinated O atoms bound to two V atoms.

8. Conclusions

This study highlights the limited effectiveness of CMD in accurately decomposing the various oxidation states of vanadium in VP50 glass. Instead, it showcases the superior accuracy of Born-Oppenheimer molecular dynamics (BOMD) in quantitatively describing the chemical speciation and structure of VP50 glass. By

performing a detailed comparison with experimental data, we found that BOMD accurately determines the final composition of V oxidation states without any a priori information, except for the total O content. BOMD also provides an accurate description of the local electronic and bonding environment around both P and V sites, allowing for a clearer signature of single V–O and double V=O bonds, and an overall improved description of the distribution of VO_n coordinating polyhedra. Furthermore, our study includes a thorough analysis of bond angle distributions, order and connectivity parameters, and local bonding features based on Wannier functions formalism. Overall, our findings provide a deeper understanding of VP50 glass paving the way to the development of future (machine learning) interatomic potentials stemming from first-principles data and expect to bring quantitative comprehension and design of VP-based amorphous materials.

Acknowledgement

Calculations were performed by using resources from GENCI (Grand Equipment National de Calcul Intensif; grants n. A0140807670, A0120807670, A0140912441 and A0120912441). The authors would like to acknowledge the High Performance Computing Center of the University of Strasbourg for supporting this work by providing scientific support and access to computing resources. Part of the computing resources were funded by the Pole HPC Équipe@Meso (Program Investissements d'Avenir) and the CPER Alsacalcul/Big Data. We acknowledge financial support from the Agence Nationale de la Recherche (ANR) within the framework of the project AMSES (ANR-20-CE08-0021). We also acknowledge the Interdisciplinary Thematic Institute QMat, as part of the ITI 2021-2028 program of the University of Strasbourg, CNRS and Inserm, as supported by IdEx Unistra (ANR-10-IDEX 0002), and by SFRI STRA'US project (ANR-20-SFRI-0012 and ANR-11-LABEX-0058-NIE-ANR-17-EURE-0024) under the framework of the French Investments for the Future Program.

Data availability

Representative trajectory files of VP50 models obtained by CMD and BOMD (PBE0) are available at the European Center of Excellence Novel Materials Discovery (CoE-NOMAD) repository [80].

References

[1] F. Kong, X. Liang, L. Yi, X. Fang, Z. Yin, Y. Wang, R. Zhang, L. Liu, Q. Chen, M. Li, et al., Multi-electron reactions for the synthesis of a vanadium-based amorphous material as lithium-ion battery cathode with high specific capacity, Energy 219 (2021) 119513.

[2] E. Boivin, J.-N. Chotard, C. Masquelier, L. Croguennec, Towards reversible high-voltage multi-electron reactions in alkali-ion batteries using vanadium phosphate positive electrode materials, Molecules 26 (2021) 1428.

[3] K. Nagamine, T. Honma, T. Komatsu, Selective synthesis of Lithium Ion-Conductive β-$LiVOPO_4$ crystals via Glass–Ceramic Processing, J. Am. Ceram. Soc. 91 (2008) 3920–3925.

[4] G. Delaizir, V. Seznec, P. Rozier, C. Surcin, P. Salles, M. Dollé, Electrochemical performances of vitreous materials in the system Li_2O–V_2O_5–P_2O_5 as electrode for lithium batteries, Solid State Ionics 237 (2013) 22–27.

[5] S. Afyon, F. Krumeich, C. Mensing, A. Borgschulte, R. Nesper, New high capacity cathode materials for rechargeable li-ion batteries: vanadate-borate glasses, Scientific reports 4 (2014) 7113.

[6] M. Kindle, Y. Cha, J. S. McCloy, M.-K. Song, Alternatives to cobalt: vanadate glass and glass-ceramic structures as cathode materials for rechargeable lithium-ion batteries, ACS Sustain. Chem. Eng. 9 (2021) 629–638.

[7] N. A. Chernova, M. F. V. Hidalgo, C. Kaplan, K. Lee, I. Buyuker, C. Siu, B. Wen, et al., Vanadyl phosphates A_xVOPO_4 (A= Li, Na, K) as multielectron cathodes for alkali-ion batteries, Adv. Energy Mater. 10 (2020) 2002638.

[8] Y. Xie, F. Gu, Q. Wang, M. Shui, J. Shu, Deep insight into the defect structure, lithium diffusion kinetics and deintercalation study on β-$LiVOPO_4$ cathode material by atomistic simulation method, J. Energy Storage 45 (2022) 103706.

[9] U. Hoppe, N. Wyckoff, M. Schmitt, R. Brow, A. Schöps, A. Hannon, Structure of V_2O_5–P_2O_5 glasses by X-ray and neutron diffraction, J. Non-Cryst. Solids 358 (2012) 328–336.

[10] U. Hoppe, R. Kranold, E. Gattef, An X-ray diffraction study of the structure of vitreous V_2O_5, Solid State Commun. 108 (1998) 71–76.

[11] U. Hoppe, A. Ghosh, S. Feller, A. Hannon, D. Keen, J. Neuefeind, Structural units of binary vanadate glasses by X-ray and neutron diffraction, J. Non-Cryst. Solids 572 (2021) 121120.

[12] A. Chrissanthopoulos, C. Pouchan, G. Papatheodorou, Structural investigation of vanadium-sodium metaphosphate glasses, Zeitschrift für Naturforschung A 56 (2001) 773–776.

[13] G. Tricot, H. Vezin, Description of the intermediate length scale structural motifs in sodium vanado-phosphate glasses by magnetic resonance spectroscopies, J. Phys. Chem. C 117 (2013) 1421–1427.

[14] G. Tricot, L. Montagne, L. Delevoye, G. Palavit, V. Kostoj, Redox and structure of sodium-vanadophosphate glasses, J. Non-Cryst. Solids 345 (2004) 56–60.

[15] X. Lu, L. Deng, S. A. Saslow, H. Liu, C. J. Benmore, B. P. Parruzot, J. T. Reiser, S. H. Kim, J. V. Ryan, J. D. Vienna, et al., Vanadium oxidation states and structural role in aluminoborosilicate glasses: an integrated experimental and molecular dynamics simulation study, J. Phys. Chem. B 125 (2021) 12365–12377.

[16] A. Raskovalov, N. Saetova, I. Popov, Structural changes in V_2O_5-P_2O_5 glasses: non-constant force field molecular dynamics and IR spectroscopy, Chim. Techno Acta 8 (2021) 20218211.

[17] M. Nabavi, C. Sanchez, J. Livage, Structure and properties of amorphous V2O5, Philos. Mag. B 63 (1991) 941–953.

[18] G. Giuli, E. Paris, J. Mungall, C. Romano, D. Dingwell, V

oxidation state and coordination number in silicate glasses by XAS, Am. Mineral. 89 (2004) 1640–1646.
[19] F. Benzi, G. Giuli, S. Della Longa, E. Paris, Vanadium k-edge XANES in vanadium-bearing model compounds: a full multiple scattering study, J. Synchrotron Radiat. 23 (2016) 947–952.
[20] G. Ori, M. Montorsi, A. Pedone, C. Siligardi, Insight into the structure of vanadium containing glasses: a molecular dynamics study, J. Non-Cryst. Solids 357 (2011) 2571–2579.
[21] G. Broglia, C. Mugoni, J. Du, C. Siligardi, M. Montorsi, Lithium vanado-phosphate glasses: Structure and dynamics properties studied by molecular dynamics simulations, J. Non-Cryst. Solids 403 (2014) 53–61.
[22] J. Du, M. Montorsi, S. Barbi, X. Lu, Rare earth and transition metal containing glasses, Atomistic Simulations of Glasses: Fundamentals and Applications (2022) 367–438.
[23] L. Deng, X. Lu, J. D. Vienna, J. Du, Structures of vanadium-containing silicate and borosilicate glasses: Vanadium potential development and MD simulations, J. Non-Cryst. Solids 575 (2022) 121223.
[24] A. Pedone, M. Bertani, L. Brugnoli, A. Pallini, Interatomic potentials for oxide glasses: Past, present, and future, J. Non-Cryst Solids X (2022) 100115.
[25] U. Hoppe, R. Kranold, A reverse monte carlo study of the structure of vitreous V_2O_5, Solid state commun. 109 (1999) 625–630.
[26] J. Kornatowski, B. Wichterlova, M. Rozwadowski, W. Baur, Simultaneous occurrence of differently coordinated framework heteroatoms in one zeolite: MFI type vanadium silicalite, KVS-5., in: Studies in Surface Science and Catalysis, volume 84, Elsevier, 1994, pp. 117–124.
[27] L. Bogomolova, V. Jachkin, N. Krasil'nikova, EPR study of vanadium-containing amorphous silica formed by sol–gel method, J. Non-Cryst. Solids 241 (1998) 13–26.
[28] M. Montorsi, G. Broglia, C. Mugoni, Structural insight into transition metal oxide containing glasses by molecular dynamic simulations, Molecular Dynamics Simulations of Disordered Materials: From Network Glasses to Phase-Change Memory Alloys (2015) 181–213.
[29] F. Benzi, E. Paris, S. Della Longa, C. Mugoni, C. Siligardi, G. Giuli, V K-Edge XANES Full Multiple Scattering Study of V-Bearing Phosphate Glasses, in: Synchrotron Radiation Science and Applications: Proceedings of the 2019 Meeting of the Italian Synchrotron Radiation Society—Dedicated to Carlo Lamberti, Springer, 2021, pp. 219–231.
[30] P. Y. Zavalij, M. S. Whittingham, Structural chemistry of vanadium oxides with open frameworks, Acta Cryst. 55 (1999) 627–663.
[31] M. Schindler, F. C. Hawthorne, W. H. Baur., Crystal chemical aspects of vanadium: polyhedral geometries, characteristic bond valences, and polymerization of (VOn) polyhedra., Chem. Mater. 12 (2000) 1248–1259.
[32] S. Boudin, A. Guesdon, A. Leclaire, M.-M. Borel., Review on vanadium phosphates with mono and divalent metallic cations: syntheses, structural relationships and classification, properties., Int. J. Inorg. Chem. 2 (2000) 561–579.
[33] A. Pedone, G. Malavasi, M. C. Menziani, A. N. Cormack, U. Segre, A new self-consistent empirical interatomic potential model for oxides, silicates, and silica-based glasses, J. Phys. Chem. B 110 (2006) 11780–11795.
[34] M. Bertani, M. C. Menziani, A. Pedone, Improved empirical force field for multicomponent oxide glasses and crystals, Phys. Rev. Mater. 5 (2021) 045602.
[35] A. Pedone, G. Malavasi, M. C. Menziani, U. Segre, A. N. Cormack, Molecular dynamics studies of stress- strain behavior of silica glass under a tensile load, Chem. Mater. 20 (2008) 4356–4366.
[36] A. Pedone, Properties calculations of silica-based glasses by atomistic simulations techniques: a review, J. Phys. Chem. C 113 (2009) 20773–20784.
[37] I. Todorov, W. Smith, U. Cheshire, The DL POLY 4 user manual, STFC, STFC Daresbury Laboratory, Daresbury, Warrington, Cheshire, WA4 4AD, United Kingdom, version 4 (2011).
[38] W. G. Hoover, Canonical dynamics: Equilibrium phase-space distributions, Phys. Rev. A 31 (1985) 1695–1697. URL: https://link.aps.org/doi/10.1103/PhysRevA.31.1695. doi:10.1103/PhysRevA.31.1695.
[39] S. Nosé, A molecular dynamics method for simulations in the canonical ensemble, Mol. Phys. 52 (1984) 255–268.
[40] S. Nosé, A unified formulation of the constant temperature molecular dynamics methods, J. Chem. Phys. 81 (1984) 511–519.
[41] T. Kühne, M. Iannuzzi, M. D. Ben, V. Rybkin, P. Seewald, F. Stein, T. Laino, R. Khaliullin, O. Schütt, F. Schiffmann, Cp2k: An electronic structure and molecular dynamics software package - quickstep: Efficient and accurate electronic structure calculations, J. Chem. Phys. 152 (2020) 1194103.
[42] J. VandeVondele, J. Hutter, Gaussian basis sets for accurate calculations on molecular systems in gas and condensed phases, J. Chem. Phys. 127 (2007) 114105.
[43] S. Goedecker, M. Teter, J. Hutter, Separable dual-space gaussian pseudopotentials, Phys. Rev. B 54 (1996) 1703.
[44] J. P. Perdew, K. Burke, M. Ernzerhof, Generalized gradient approximation made simple, Phys. Rev. Lett. 77 (1996) 3865.
[45] C. Adamo, V. Barone, Toward reliable density functional methods without adjustable parameters: The pbe0 model, J. Chem. Phys. 110 (1999) 6158–6170.
[46] M. Ernzerhof, G. Scuseria, Assessment of the perdew.burke.ernzerhof exchange-correlation functional, J. Chem. Phys. 110 (1999) 5029.
[47] M. Seth, T. Ziegler, Range-separated exchange functionals with slater-type functions, J. Chem. Theory Comput. 8 (2012) 901–907.
[48] A. Saúl, G. Radtke, Density functional approach for the magnetism of β-$TeVO_4$, Phys. Rev. B 89 (2014) 104414.
[49] R. Resta, S. Sorella, Electron localization in the insulating state, Phys. Rev. Lett. 82 (1999) 370.
[50] N. Marzari, D. Vanderbilt, Maximally localized generalized wannier functions for composite energy bands, Phys. Rev. B 56 (1997) 12847.
[51] G. H. Wannier, The structure of electronic excitation levels in insulating crystals, Phys. Rev. 52 (1937) 191.
[52] M. Boero, M. Parrinello, K. Terakura, T. Ikeshoj, C. C. Liew, First-principles molecular-dynamics simulations of a hydrated electron in normal and supercritical water, Phys. Rev. Lett. 90 (2003) 226403.
[53] M. Sharma, Y. Wu, R. Car, Ab initio molecular dynamics with maximally localized wannier functions, Int. J. Quantum Chem. 95 (2003) 821–829.
[54] R. Raghvender, A. Bouzid, S. Cadars, D. Hamani, P. Thomas, O. Masson, Structure of amorphous teo 2 revisited: A hybrid functional ab initio molecular dynamics study, Phys. Rev. B 106 (2022) 174201.
[55] A. Bouzid, G. Ori, M. Boero, E. Lampin, C. Massobrio, Atomic-scale structure of the glassy $Ge_2Sb_2Te_5$ phase change material: A quantitative assessment via first-principles molecular dynamics., Phys. Rev. B 96 (2017) 224204.
[56] G. Ori, C. Massobrio, A. Bouzid, M. Boero, B. Coasne, Surface of glassy GeS_2: A model based on a first-principles approach, Phys. Rev. B 90 (2014) 045423.
[57] P. Chaurand, J. Rose, V. Briois, M. Salome, O. Proux, V. Nassif,

L. Olivi, J. Susini, J.-L. Hazemann, B. J.-L., New methodological approach for the vanadium K-edge X-ray absorption near-edge structure interpretation: Application to the speciation of vanadium in oxide phases from steel slag, J. Phys. Chem. B 111 (2007) 5101–5110.

[58] G. Calas, J. Petiau, Structure of oxide glasses: spectroscopic studies of local order and crystallochemistry. geochemical implications, Bull. Min. 106 (1983) 33–55.

[59] R. S. Mulliken, Electronic population analysis on LCAO–MO molecular wave functions. i, J. Chem. Phys. 23 (1955) 1833–1840.

[60] R. F. Bader, M. E. Stephens, Spatial localization of the electronic pair and number distributions in molecules, J. Am. Chem. Soc. 97 (1975) 7391–7399.

[61] A. K. Rappe, W. A. Goddard III, Charge equilibration for molecular dynamics simulations, J. Phys. Chem. 95 (1991) 3358–3363.

[62] K. Han, C. Hwang, D. Kim, D. Gwoo, T. Kim, W. Choi, K. Kee, J. Kim, B. Ryu, Effects of substituting b_2o_3 for p_2o_5 on the structures and properties of v_2o_5-p_2o_5 glass systems, Electron. Mater. Lett. 8 (2012) 655–658.

[63] P. S. Salmon, A. Zeidler, Networks under pressure: the development of in situ high-pressure neutron diffraction for glassy and liquid materials, J. Phys.: Condens. Matter. 27 (2015) 133201.

[64] T. Faber, J. Ziman, A theory of the electrical properties of liquid metals: Iii. the resistivity of binary alloys, Philos. Mag. 11 (1965) 153–173.

[65] C. Massobrio, Amorphous materials via atomic-scale modeling, in: The Structure of Amorphous Materials using Molecular Dynamics, 2053-2563, IOP Publishing, (2022), pp. 2–1 to 2–27.

[66] V. F. Sears, Neutron scattering lengths and cross sections, Neutron news 3 (1992) 26–37.

[67] C. T. Chantler, Theoretical form factor, attenuation, and scattering tabulation for z= 1–92 from e= 1–10 ev to e= 0.4–1.0 mev, J. Phys. Chem. Ref. Data 24 (1995) 71–643.

[68] A. C. Wright, The comparison of molecular dynamics simulations with diffraction experiments, J. Non-Cryst. Solids 159 (1993) 264–268.

[69] U. Hoppe, G.Walter, R. Kranold, D. Stachel, Structural specifics of phosphate glasses probed by diffraction methods: a review., J. Non-Cryst. Solids 264 (2000) 29–47.

[70] T. Aoyagi, S. Kohara, T. Naito, Y. Onodera, M. Kodama, T. Onodera, D. e. a. Takamatsu, Controlling oxygen coordination and valence of network forming cations, Scientific reports 10 (2020) 1–12.

[71] J. R. Errington, P. G. Debenedetti, Relationship between structural order and the anomalies of liquid water, Nature 409 (2001) 318–321.

[72] A. Bouzid, C. Massobrio, M. Boero, G. Ori, K. Sykina, E. Furet., Role of the van der waals interactions and impact of the exchange-correlation functional in determining the structure of glassy $GeTe_4$., Phys. Rev. B 92 (2015) 134208.

[73] A. Bouzid, T.-L. Pham, Z. Chaker, M. Boero, C. Massobrio, Y.-H. Shin, G. Ori, Quantitative assessment of the structure of $Ge_{20}Te_{73}I_7$ chalcohalide glass by first-principles molecular dynamics, Phys. Rev. B 103 (2021) 094204.

[74] M. Guerboub, S. D. Wansi Wendji, C. Massobrio, A. Bouzid, M. Boero, G. Ori, E. Martin, Impact of the local atomic structure on the thermal conductivity of amorphous $Ge_2Sb_2Te_5$, J. Chem. Phys. 158 (2023) 084504.

[75] R. K. Brow, The structure of simple phosphate glasses., J. Non-Cryst. Solids. 263 (2000) 1–28.

[76] L. Zheng, X. Yang, J. Li, R. Yang, H. Qu, X. Guo, S. Huang, S. Zhang, DFT calculation of structures and electronic characteristic of $VOPO_4$ polymorphs, Phys. Scripta 97 (2022) 105805.

[77] P. L. Silvestrelli, E. Martin, M. Boero, A. Bouzid, G. Ori, C. Massobrio, Atomic structure of glassy $GeTe_4$ as a playground to assess the performances of density functional schemes accounting for dispersion forces, J. Phys. Chem. B 124 (2020) 11273–11279.

[78] N. Marzari, A. A. Mostofi, J. R. Yates, I. Souza, D. Vanderbilt, Maximally localized wannier functions: Theory and applications, Reviews of Modern Physics 84 (2012) 1419.

[79] L. Pauling, The Nature of the Chemical Bond 3-rd ed Ithaca, New York: Cornell Univer (1960).

[80] Data will be deposited and available at NOMAD data repository with doi coordinates, once the peer-review process will be finalized., 2023. URL: `DOI TO BE UPDATED`.